PHOTONICS Research

Light rays and waves on geodesic lenses

Lin Xu,[1,4,†] Xiangyang Wang,[2,†] Tomáš Tyc,[3,5,†] Chong Sheng,[2] Shining Zhu,[2] Hui Liu,[2,6] and Huanyang Chen[1,7]

[1]Institute of Electromagnetics and Acoustics and Key Laboratory of Electromagnetic Wave Science and Detection Technology, Xiamen University, Xiamen 361005, China
[2]National Laboratory of Solid State Microstructures and School of Physics, Collaborative Innovation Center of Advanced Microstructures, Nanjing University, Nanjing 210093, China
[3]Department of Theoretical Physics and Astrophysics, Masaryk University, Kotlarska 2, 61137 Brno, Czech Republic
[4]Institutes of Physical Science and Information Technology & Key Laboratory of Opto-Electronic Information Acquisition and Manipulation of Ministry of Education, Anhui University, Hefei 230601, China
[5]e-mail: tomtyc@physics.muni.cz
[6]e-mail: liuhui@nju.edu.cn
[7]e-mail: kenyon@xmu.edu.cn

Received 18 April 2019; revised 19 August 2019; accepted 3 September 2019; posted 11 September 2019 (Doc. ID 365526); published 28 October 2019

Starting from well-known absolute instruments that provide perfect imaging, we analyze a class of rotationally symmetric compact closed manifolds, namely, geodesic lenses. We demonstrate with a numerical method that light rays confined on geodesic lenses form closed trajectories, and that for optical waves, the spectrum of a geodesic lens is (at least approximately) degenerate and equidistant. Moreover, we fabricate two geodesic lenses in micrometer and millimeter scales and observe curved light rays along the geodesics. Our experimental setup may offer a new platform to investigate light propagation on curved surfaces.

https://doi.org/10.1364/PRJ.7.001266

1. INTRODUCTION

Absolute instruments (AIs) in optics mean devices that bring stigmatically an infinite number of light rays from a source to its image, which can perform perfect imaging in the perspective of geometrical optics [1,2]. Two well-known examples of AIs are a plane mirror and Maxwell's fish-eye lens [with gradient refractive index profile; see Fig. 1(a)]. Actually, there are a lot of AIs, such as the Eaton lens, Luneburg lens, and invisible lens [3]. The invisible lens has a spherically symmetric index profile that forces light rays to make loops around its center and then propagate in their original directions, which makes it invisible. Recently, one author proposed a general method to design AIs with the help of the Hamilton–Jacobi equation [4], which has flourished in the family of AIs. No matter how perfectly stigmatic the geometrical-optics image might be, in the wave-optics regime, the resolution is always limited by diffraction. Owing to this limitation, "perfect imaging" in the perspective of geometrical optics and wave optics is quite different [3]. As far as we know, the only AI in both perspectives is Pendry's slab [5]. However, the frequency spectrum of other AIs has been investigated by numerical method [6,7] and the Wentzel–Kramers–Brillouin (WKB) approximation [8,9]. It is found that their spectrum is (at least approximately) degenerate and equidistant, which contributes to periodical evolution of waves in AIs [6,8].

With a conformal coordinate transformation, AIs with cylindrical-symmetry refractive index profiles in two-dimensional (2D) space can be connected to curved surfaces with rotational-symmetry embedding in three-dimensional (3D) space in the perspective of geometrical optics [10,11]. Such surfaces are usually called geodesic lenses (GLs) corresponding to AIs. For compact GLs, their geodesics are all closed. Therefore, all light rays on compact GLs follow closed trajectories that correspond to the perfect imaging of AIs [12]. However, for wave optics, it has not been clear so far whether the spectra of GLs share the properties of spectra of AIs, namely, whether they are (at least approximately) degenerate and equidistant or not.

For light propagation on a 3D curved surface, such as a sphere, hyperbolic surface, and paraboloid, there are several important theoretical works and experimental works [13–18]. In 2008, light constrained to a 3D curved surface via a possible nonlinear film waveguide was proposed theoretically [13]. It was shown that wave propagation on 3D curved surfaces was approximated to the one in a 2D plane with a refractive-index profile. Later in 2010, the evolution of light on 3D curved surfaces was experimentally studied in centimeter scale [14]. Periodic refocusing, self-imaging, and diffractionless propagation on sphere surfaces were observed, while two-beam interference on hyperbolic surfaces was first realized. Recently,

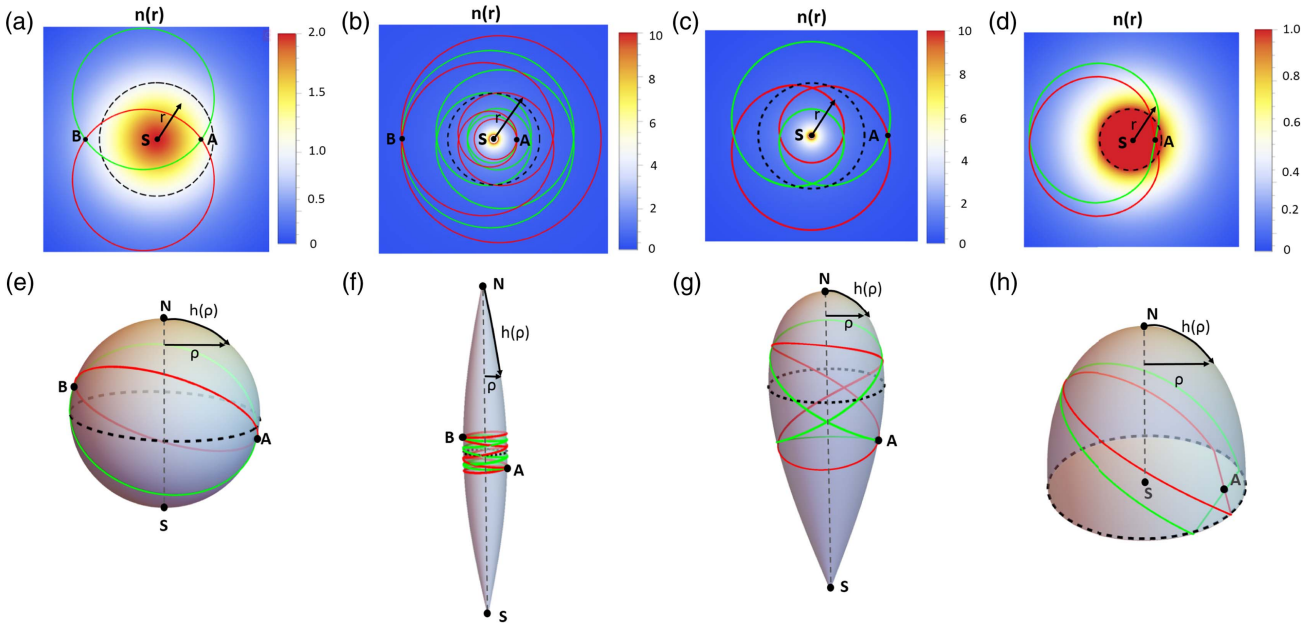

Fig. 1. AIs (upper row) and corresponding GLs (lower row) with rotational symmetry. In AIs, the center of each lens is marked with S. The position vector is denoted with $\boldsymbol{r}$. The angle parameter θ is omitted for simplification because of rotational symmetry of AIs and GLs. Contour plots show refractive index profile of $n(r)$. The presented AIs are Maxwell's fish-eye lens (a), generalized Maxwell's fish-eye lens with $M = 5$ (b), extended invisible lens (c), and inverse invisible lens (d). The corresponding geodesic lenses are sphere (a), spindle with $M = 5$ (b), Tannery's pear (c), and truncated Tannery's pear (d). On GLs, the axis of rotational symmetry is denoted by a dashed line, which connects north (N) pole and south (S) pole. ρ is the radial coordinate, and $h(\rho)$ is the length measured along the meridian from N pole on the geodesic surface. Light rays starting from point A form closed trajectories shown in different colors. S poles are mapped from the centers S of AIs, while N poles correspond to the infinities of AIs. Dashed black circles of AIs are places with refractive index of unity at radius of r_0, which are equivalent to those of GLs.

shape-preserving accelerating electromagnetic wave packets on sphere surfaces and hyperbolic surfaces were further investigated in both theory [15] and experiment [16]. Also, the theoretical and experimental research of Hanbury Brown and Twiss measurements on curved space was also reported [17]. Moreover, the study of the control of light on paraboloid surfaces was carried out on nanophotonic structures [18]. Nevertheless, there is no experiment reported on non-spherical GLs with perfect imaging functionality, which is usually not possible for general curved surfaces.

In this paper, we first introduce GLs and confirm with a numerical method that the spectra of compact GLs are (at least approximately) degenerate and equidistant. After that, we fabricate part of a spindle in micrometer scale and a sphere in millimeter scale, where curved light rays along the geodesics are observed.

2. GEODESIC LENSES CONSTRUCTED FROM ABSOLUTE INSTRUMENTS

AIs with cylindrical-symmetry refractive index profiles denoted by $n(r)$ have been widely studied [3,11,12]. We present a Maxwell's fish-eye lens [19], a generalized Maxwell's fish-eye lens [3] with $M = 5$, an extended invisible lens [20], and an inverse invisible lens [12] with contour plots in Figs. 1(a)–1(d), respectively. The invisible lens has a refractive index given by an implicit formula:

$$(r/r_0)n^{3/2} + (r/r_0)n^{1/2} - 2 = 0, \tag{1}$$

in the region $r < r_0$, while for $r > r_0$, the index is unity. The inverse invisible lens, on the other hand, has the index given by Eq. (1) for $r > r_0$ and $n = 1$ for $r < r_0$. The extended invisible lens has the index profile given by Eq. (1) for all r. Both the inverse and extended invisible lenses are absolute instruments where light rays form closed loops. Hence, an invisible lens is a finite device, while an extended or inverse one is infinite. The center of each lens is marked with S. The position vector is denoted with $\boldsymbol{r}$. Point sources at position A have either a perfect image at position B [see Figs. 1(a) and 1(b)] or have a self-image at position A [see Figs. 1(c) and 1(d)]. By using Hamilton's equation of optics, we can find all the trajectories in AIs, as shown in red and green closed curves [21]. There is a conformal coordinate transformation between AIs and GLs [11], written as

$$\rho = n(r)r, \qquad \mathrm{d}h = n(r)\mathrm{d}r, \tag{2}$$

where ρ is radial coordinate, and h is the length measured along the meridian from the north poles of the GLs. Equation (2) enables to construct a GL from a given index profile of an AI. We have constructed four such GLs that correspond to the above AI index profiles and are shown in Figs. 1(e)–1(h): the sphere, spindle [12] (we use this name according to its shape), Tannery's pear [22], and truncated Tannery's pear [23], respectively. The list of these Gls along with the corresponding AIs is given in Table 1. We will further investigate theoretically the properties of light waves in GLs

Table 1. Description of Four AIs and Corresponding GLs with Spectrum

Lens	Refractive Index Profile	Geodesic Lens	Description of Geodesic Lens	Spectrum
Maxwell's fish-eye lens	$n(r)=\frac{2}{1+(r/r_0)^2}$	Sphere	$h(\rho)=\arcsin(\rho)$	$\frac{\omega_{Nm}r_0}{c}=\sqrt{(N+m)(N+m+1)}\approx N+m+0.5$
Generalized Maxwell's fish-eye lens	$n(r)=\frac{2(r/r_0)^{1/M-1}}{1+(r/r_0)^{2/M}}$, $M=2,3,4,\ldots$	Spindle	$h(\rho)=\arcsin(M\rho)$, $M=2,3,4,\ldots$	$\frac{\omega_{Nm}r_0}{c}=\frac{\sqrt{(N+M\cdot m)(N+M\cdot m+1)}}{M}\approx\frac{N+0.5}{M}+m$
Extended invisible lens	$(r/r_0)n^{3/2}+(r/r_0)n^{1/2}-2=0$	Tannery's pear	$h_1(\rho)=-\rho+2\arcsin(\rho)$, $h_2(\rho)=\rho+2\arcsin(\rho)$	$\frac{\omega_{Nm}r_0}{c}\approx\frac{N+0.5}{2}+m$
Inverse invisible lens	$(r/r_0)n^{3/2}+(r/r_0)n^{1/2}-2=0$ for $r>r_0$; $n=1$ for $r<r_0$	Truncated Tannery's pear	$h_1(\rho)=-\rho+2\arcsin(\rho)$, $h_2(\rho)=2+\pi-\rho$	$\frac{\omega_{Nm}r_0}{c}\approx N+m+0.5$

mentioned in Fig. 1 and Table 1, and the first two of them also experimentally.

3. LIGHT RAYS AND WAVES ON GEODESIC LENSES

An important thing is that the local refractive index profile on GLs is constant (and equal to unity), which is quite different from that of AIs. Light trajectories on GLs can be simply obtained by Eq. (2) from those in the corresponding AIs. Since we know the shape of GLs, we can also find their geodesics by solving the geodesic equations, namely,

$$\frac{\mathrm{d}^2x^\lambda}{\mathrm{d}\xi^2}+\Gamma^\lambda_{\mu\nu}\frac{\mathrm{d}x^\mu}{\mathrm{d}\xi}\frac{\mathrm{d}x^\nu}{\mathrm{d}\xi}=0, \tag{3}$$

where ξ is the parameter of geodesics, $\Gamma^\lambda_{\mu\nu}$ is the Christoffel symbols of coordinate system $\{x^\lambda;\lambda=1,2\}$. Those geodesics are shortest paths in GLs, which correspond to light trajectories. Because of rotational-symmetrical $\rho(h)$ of GLs, we find that the Christoffel symbols are written as

$$\Gamma^\lambda_{\mu\nu}=\begin{pmatrix}\begin{pmatrix}0&0\\0&-\rho(h)\rho'(h)\end{pmatrix}_{\mu\nu}\\ \begin{pmatrix}0&\frac{\rho'(h)}{\rho(h)}\\ \frac{\rho'(h)}{\rho(h)}&0\end{pmatrix}_{\mu\nu}\end{pmatrix}_\lambda, \tag{4}$$

where we use the coordinates $\{h,\theta\}$ for $\{x^\lambda;\lambda=1,2\}$. All the geodesic equations in Eq. (3) are

$$\begin{cases}h''(\xi)-\rho[h(\xi)]\rho'[h(\xi)]\theta'(\xi)\theta'(\xi)=0,\\ \theta''(\xi)+2\frac{\rho'[h(\xi)]}{\rho[h(\xi)]}h'(\xi)\theta'(\xi)=0.\end{cases} \tag{5}$$

By solving Eq. (5) with $\rho(h)$ and given initial conditions, we can find their geodesics, shown in Figs. 1(e)–1(h) with red and green closed curves.

Since the transformation of Eq. (2) is conformal, it preserves the angle of two light trajectories in AIs to that of their images on GLs [12], which might find application in conformal transformation optics.

The frequency spectra of AIs have a distinctive feature: they are, at least approximately, degenerate and equidistant. This has been shown by solving the Helmholtz equation by numerical methods [6] as well as using the WKB approximation [4,8]. For GLs, the Helmholtz equation in curved 2D surfaces is written as

$$\tilde{\nabla}^2\psi+\frac{\omega^2}{c^2}\psi=0, \tag{6}$$

where ψ is a wave function, c is the speed of light, ω is eigen-frequency, and $\tilde{\nabla}^2$ is Laplacian on a curved surface. Because of the rotational symmetry of GLs, we can make an ansatz of the wave function, namely,

$$\psi(h,\varphi)=R(h)e^{im\varphi}, \tag{7}$$

where $m\in N$ is an angular periodic number, and R is a function depending on h. Substituting Eq. (7) into Eq. (6), we get

$$\frac{\partial^2R}{\partial h^2}+\frac{1}{\rho}\frac{\partial\rho}{\partial h}\frac{\partial R}{\partial h}+\left(\frac{\omega^2}{c^2}-\frac{m^2}{h^2}\right)R=0. \tag{8}$$

We can solve the eigen-problem of Eq. (8) numerically. We find that ω is (at least approximately) degenerate with m. The solutions of Eq. (8) with finite-value boundary conditions can be numbered by a non-negative integer N, which represents the number of nodes of the function $R(h)$. Therefore, we can denote the wave function and its eigen-frequency with ψ_{Nm} and ω_{Nm}, respectively. These results are summarized in the column "Spectrum" of Table 1. Moreover, ω_{Nm} can be written as

$$\omega_{Nm}=a\cdot s_{Nm}+b, \tag{9}$$

where a, b are constants, and s_{Nm} is an integer for all modes ψ_{Nm}. The integer numbers N and m represent the modes in a natural way: N determines the number of zeros of eigenfunctions in the latitude direction, while m determines the phase change (in multiples of 2π) when encircling the geodesic lens along a latitude line. It implies that the spectra of GLs are (at least approximately) degenerate and equidistant. We plot some typical wave functions on each GL, as shown in Fig. 2.

4. EXPERIMENTAL FABRICATION OF TWO GEODESIC LENSES

To verify the trajectories in geodesic lenses, we performed two experiments involving light beams propagating on a curved surface in 3D space. One geodesic lens is part of a spindle corresponding to a generalized Maxwell's fish-eye lens with $M=5$. The other is a sphere corresponding to a Maxwell's fish-eye lens. The experiment is achieved based on a polymethyl methacrylate (PMMA) waveguide, which is fabricated through the self-assembling of polymer solutions on solid substrates [24,25].

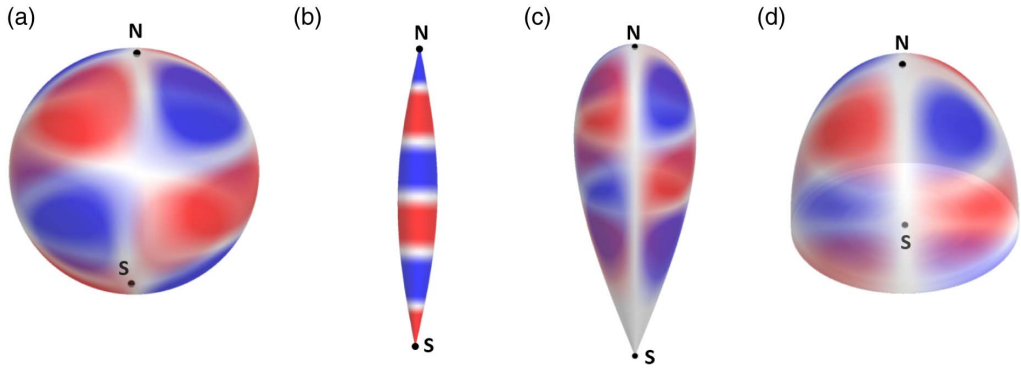

Fig. 2. Real part of the modes with different indices N and m: (a) ψ_{22} on sphere, (b) ψ_{50} on spindle, (c) ψ_{22} on Tannery's pear, and (d) ψ_{22} on truncated Tannery's pear.

Our geodesic lens is a 2D waveguide with a PMMA polymer layer spin-coated on the surface of a metallic needle in spindle shape. The PMMA polymer layer has a uniform thickness of about 2 μm and is doped with the rare-earth ion Eu^{3+} to emit fluorescent light at 615 nm when illuminated with a laser beam with 460 nm wavelength. The optical measurement is based on waveguide excitation and fluorescent imaging techniques shown in Fig. 3(a). In the process, the beam is coupled through grating from the top of the sample, as shown in Fig. 3(a), and propagates in the waveguide. The fluorescent light goes through a color filter and finally is collected by a CCD camera. Figure 3(b) displays the structure of the waveguide in detail. We can take it as a bulk material with a refractive index around 1.52 on the surface. We use the spin-coating method to deposit the PMMA polymer layer on the surface of a metallic needle shape. First, we put on a hydrogen flame at a proper position under a straight silver wire. Then, the ends of the straight silver wire are pulled so that the silver wire gradually becomes tapered. Finally, the silver wire is broken into two metallic cones at some point. The details of the sample fabrication can be found in Appendix A. Figures 3(c) and 3(d) show the scanning electron microscope (SEM) image of the metallic needle shape with different scales before spin coating. Based on these figures, we can accurately obtain the parameters of the metallic needle shape. In Fig. 3(c), the height of the part of the spindle that we observed under SEM is 644 μm, and its diameter ranges from 169 μm to 346 μm. The coupling grating, i.e., the cross structure shown in Fig. 3(c), is fabricated before the spin-coating process.

In Fig. 4(a), we find that a spindle with $M = 5$ in Fig. 1(f) is exactly the shape of our metallic needle in Fig. 3(d). The edge of our sample is almost part of the outline of the spindle (in blue). A point source in the spindle has a closed trajectory in red. Figure 4(b) shows that a laser hitting the cross grating generates a coupling source on a metallic needle shape, which further results in a light trajectory on a curved surface by using

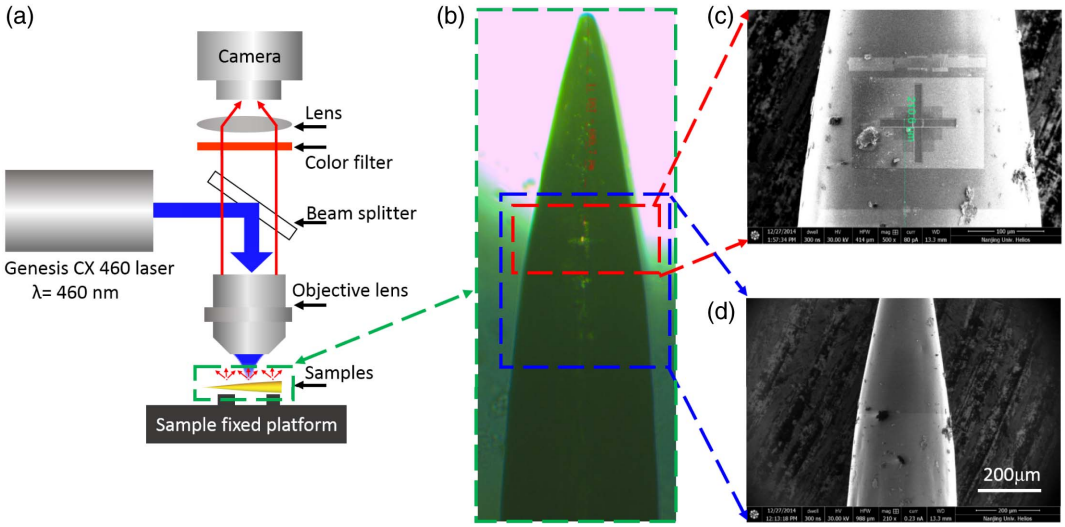

Fig. 3. Experimental setup and sample description. (a) Schematic of the observation and coupling scheme of the light to the geodesic lens. A laser beam is coupled to a 3D curved waveguide from the top and excites the rare-earth ions in the waveguide. The emitted fluorescent light at 615 nm is then collected by a CCD camera. (b) 3D curved waveguide morphology captured by a CCD camera when illuminated by white light. (c) Scanning electron microscope image of the 3D curved surface around the coupling grating (red dashed box) before spin coating. The cross structure corresponds to that displayed in (b) and is used to couple laser beams into the waveguide. (d) Scanning electron microscope image of the 3D curved surface with larger scale (blue dashed box) before spin coating. Based on this figure, one can get the accurate parameters of the 3D curved surface.

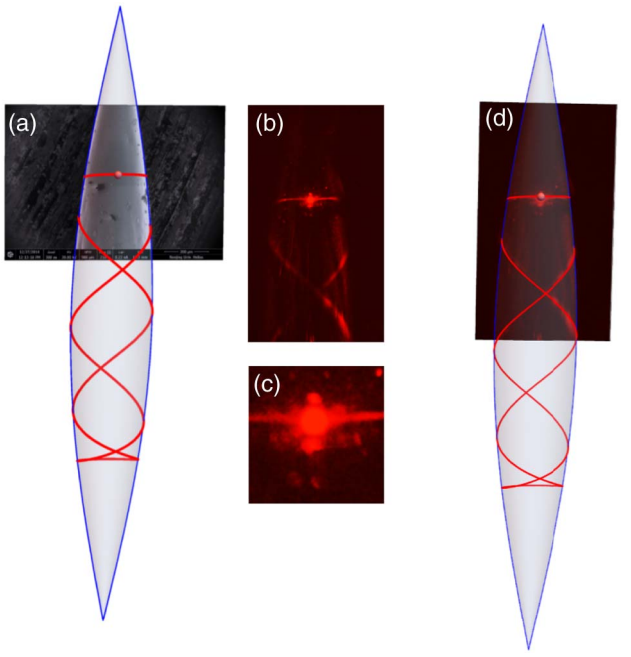

Fig. 4. Optical measurements and fitting results of light rays in a spindle with $M = 5$. (a) Fitting the shape of micro-structured metallic needle waveguide with a spindle. (b) Optical measurements on micro-structured metallic needle waveguide. (c) Enlarged drawing nearby the coupling source. (d) Fitting the light trajectory of micro-structured metallic needle waveguide with a spindle.

a CCD camera. An enlarged drawing nearby the coupling source is shown in Fig. 4(c). The details of experimental measurements can be found in Appendix B. We use the spindle in Fig. 1(f) to fit the measurement in Fig. 4(b). The observed light trajectory matches the calculated one very well, as shown in Fig. 4(d). Based on the results of the shape using SEM and light trajectories using a CCD camera, we confirm that we have fabricated part of a spindle with $M = 5$ and observed part of a closed trajectory. Similarly, we also fabricate a sphere with a radius of 1 mm in Appendix C, which is surely a well-known GL. It is noted that there is another experiment to explore the light propagation on a sphere made of BK7 glass with a radius of 12.5 mm [14]. It focuses more on curved surfaces with constant curvatures, while our work here focuses more on GLs with closed geodesics and perfect imaging functionalities.

5. CONCLUSION

To conclude, we have demonstrated with numerical methods that the light trajectories of GLs are closed and the spectra of compact GLs are (at least approximately) degenerate and equidistant. Those properties depend mainly on the differential structure of GLs embedding in the 3D space. It is noted that the toroidal surface with the genius one has a focusing property under paraxial approximation [26]. It is worth to explore whether there exist some GLs with different geniuses that could achieve perfect imaging. We further fabricate two GLs, namely, part of a spindle in micrometer scale and a sphere in millimeter scale. In these two GLs, we observe curved geodesic light trajectories. Our results may offer a new platform to investigate light propagation on curved surfaces, especially in mircophotonics or nanophotonics when combining GLs to microcavities and enhancing the Q factors. The GLs might also find applications in improving the efficiency of micro-LED technology.

APPENDIX A: SAMPLE FABRICATION

A spindle waveguide with uniform thickness was fabricated for our experiment, as depicted in Fig. 3(b) in the main text. The sample is a polymethyl methacrylate (PMMA) resist polymer layer on the surface of a metallic spindle. The fabrication process is based on a metallic wire fusion technique and

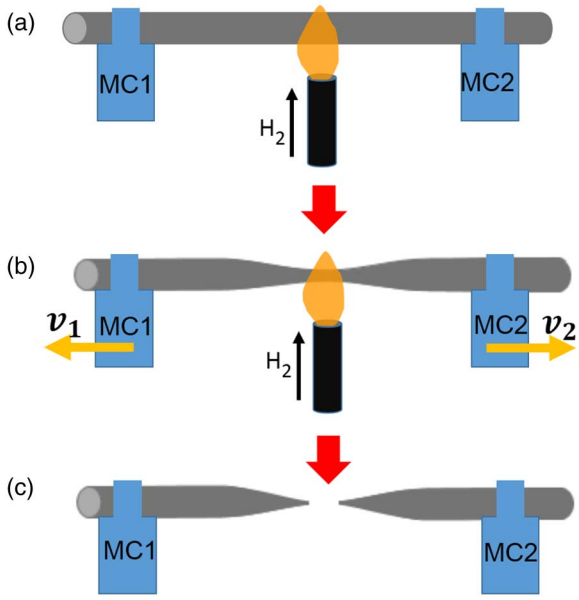

Fig. 5. Sample fabrication process. (a) Position of straight silver wire, movement console (MC), and hydrogen flame. A straight silver wire is fixed on MC1 and MC2 and then put on a hydrogen flame at a proper position. (b) Metallic wire fusion process. The ends of the straight silver wire are pulled at speeds v_1 and v_2, and the silver wire gradually becomes tapered. (c) Two obtained metallic cones. The silver wire breaks into two metallic cones at some point.

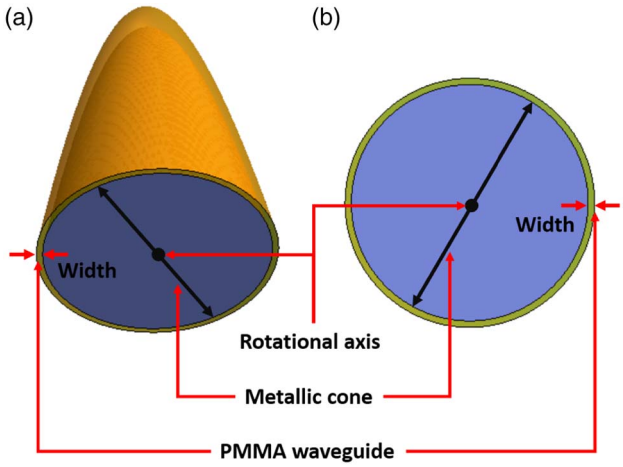

Fig. 6. (a) Sketch of a metallic waveguide. (b) Cross section of the metallic waveguide.

spin-coating technique. First, a straight silver wire with a diameter of 400 μm was put on a hydrogen flame [Fig. 5(a)]. Second, the ends of the straight silver wire were pulled at a specific speed and broke into two parts [Figs. 5(b) and 5(c)]. Third, the broken end [Figs. 3(c) and 3(d) in the main text] of the silver wire was coated with a PMMA layer, and the rare-earth ion Eu^{3+} was added to the PMMA resist to facilitate fluorescence imaging to reveal the propagation dynamics of light beams. Finally, a three-dimensional metallic waveguide, namely, a polymer layer on the surface of the broken end of the silver wire, was obtained [Fig. 3(d) in the main text]. In the experiment, the shape of the metallic spindle could be changed by controlling the pulling rate of the ends of the straight metallic wire, the materials of the metallic wire, and the distance between the silver wire and the hydrogen flame.

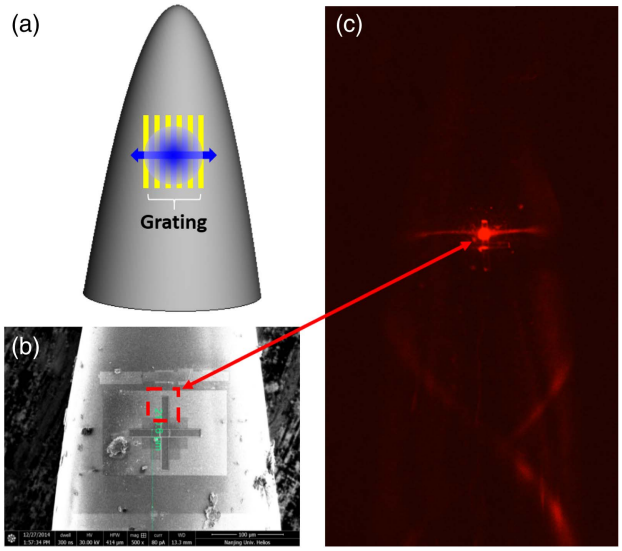

Fig. 7. (a) Sketch of the coupling grating (yellow boxes). (b) SEM image of the metallic curved surface and the coupling grating (in red dashed box) before spin-coating process. (c) Grating coupling process and optical measurement of the sample. The yellow boxes in (a) show the coupling grating, the graded blue spot represents the exciting beam, and the blue arrows show the direction of the laser beam propagating in the waveguide. The coupling grating in (a) corresponds to the red dashed box in (b), which is fabricated before spin-coating process. The red dashed box region in (b) corresponds to the grating in (c), which is indicated by the red arrows.

The polymer layer thickness and uniformity could be varied by changing the solubility of the PMMA solution, the evaporation rate of the oven, and the pulling rate, immersion rate, and cycling time of the spin coating. By changing these parameters, a spindle waveguide of the desired shape was fabricated. The thickness of the waveguide was great enough such that it effectively behaved as a bulk material with a refractive index around 1.52. A sketch of the waveguide is shown in Fig. 6. In our experiment, the light is transported only inside the polymer waveguide layer attached to the iron curved spindle. The iron is used to support the curved thin polymer layer. The laser is coupled to this layer from the grating. Since most energy of the laser is confined in the polymer layer but not iron, the influence of loss inside the iron is negligible.

APPENDIX B: EXPERIMENTAL MEASUREMENTS

As mentioned in Appendix A, a metallic waveguide was generated along the metallic curved surface by means of spin-coating technology. We then used the experimental setup [Fig. 3(a) in the main text] to measure the light propagation in the metallic waveguide. A laser beam at a wavelength of 460 nm was coupled to the waveguide by a grating with a period of 310 nm, which was fabricated on the metallic curved surface with a focused ion beam (FEI Strata FIB 201, 30 keV, 11 pA) before the spin-coating process. To better illustrate the coupling process, we made a sketch of the grating [Fig. 7(a)]. It (in the yellow boxes) corresponds to the red dashed box in Fig. 7(b), which is an SEM image of the curved surface. After the spin-coating process, a thick enough PMMA polymer layer was deposited on the surface. The blue laser beam was perpendicularly incident on the grating, and converted to the PMMA waveguide. Figure 7(c) shows the grating coupling process and the optical measurement of the metallic waveguide.

APPENDIX C: A SPHERICAL GL

Similarly, we also fabricated a sphere as shown in Fig. 8(a) under a CCD camera. The sphere is made of iron, and its radius is 1 mm. By the spin-coating method, a uniform PMMA polymer layer is formed on the sphere. A handle is attached to the sphere to fix it. A grating is etched nearby the handle to couple the laser beam into the waveguide, which results in closed trajectories on the sphere. By turning off the background illumination in Fig. 8(a), a clearer picture of a closed

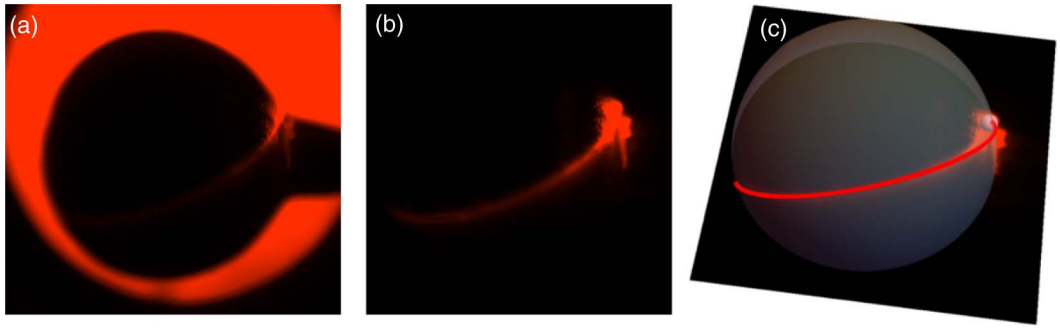

Fig. 8. Optical measurements and fitting results of light rays on a sphere. (a) CCD camera picture of micro-structured sphere waveguide. (b) Light trajectory on micro-structured sphere waveguide. (c) Fitting the light trajectory with a sphere.

light trajectory on the sphere is shown in Fig. 8(b). We also compare the experimental measurement in Fig. 8(b) with the shape in Fig. 1(e) in the main text, which demonstrates that a sphere has been fabricated and a closed light trajectory is observed.

Funding. Fundamental Research Funds for the Central Universities (20720170015); National Key Projects for Basic Researches of China (2017YFA0205700, 2017YFA0303700); National Natural Science Foundation of China (NSFC) (11874311, 11690033, 61322504, 11621091, 61425018, 11904006, 11374151); Natural Science Foundation of Anhui Province of China (1908085QA20); Czech Science Foundation (P201/12/G028).

†These authors contributed equally to this work.

REFERENCES

1. M. Born and E. Wolf, *Principles of Optics: Electromagnetic Theory of Propagation, Interference and Diffraction of Light, CUP Archive* (2000).
2. R. K. Luneburg and M. Herzberger, *Mathematical Theory of Optics* (University of California, 1964).
3. T. Tyc, L. Herzánová, M. Šarbort, and K. Bering, "Absolute instruments and perfect imaging in geometrical optics," New J. Phys. **13**, 115004 (2011).
4. T. Tyc and A. J. Danner, "Absolute optical instruments, classical superintegrability, and separability of the Hamilton-Jacobi equation," Phys. Rev. A **96**, 053838 (2017).
5. J. B. Pendry, "Negative refraction makes a perfect lens," Phys. Rev. Lett. **85**, 3966–3969 (2000).
6. T. Tyc and A. Danner, "Frequency spectra of absolute optical instruments," New J. Phys. **14**, 085023 (2012).
7. T. Tyc, H. Chen, A. Danner, and Y. Xu, "Invisible lenses with positive isotropic refractive index," Phys. Rev. A **90**, 053829 (2014).
8. T. Tyc, "Spectra of absolute instruments from the WKB approximation," New J. Phys. **15**, 065005 (2013).
9. K. Zuzaňáková and T. Tyc, "Scattering of waves by the invisible lens," J. Opt. **19**, 015601 (2016).
10. R. Rinehart, "A solution of the problem of rapid scanning for radar antennae," J. Appl. Phys. **19**, 860–862 (1948).
11. S. Cornbleet and P. Rinous, "Generalised formulas for equivalent geodesic and nonuniform refractive lenses," IEE Proc. H-Microw. Opt. Antennas **128**, 95 (1981).
12. M. Šarbort and T. Tyc, "Spherical media and geodesic lenses in geometrical optics," J. Opt. **14**, 075705 (2012).
13. S. Batz and U. Peschel, "Linear and nonlinear optics in curved space," Phys. Rev. A **78**, 043821 (2008).
14. V. H. Schultheiss, S. Batz, A. Szameit, F. Dreisow, S. Nolte, A. Tünnermann, S. Longhi, and U. Peschel, "Optics in curved space," Phys. Rev. Lett. **105**, 143901 (2010).
15. R. Bekenstein, J. Nemirovsky, I. Kaminer, and M. Segev, "Shape-preserving accelerating electromagnetic wavepackets in curved space," Phys. Rev. X **4**, 011038 (2014).
16. A. Patsyk, M. A. Bandres, R. Bekenstein, and M. Segev, "Observation of accelerating wave packets in curved space," Phys. Rev. X **8**, 011001 (2018).
17. V. H. Schultheiss, S. Batz, and U. Peschel, "Hanbury Brown and Twiss measurements in curved space," Nat. Photonics **10**, 106–110 (2016).
18. R. Bekenstein, Y. Kabessa, Y. Sharabi, O. Tal, N. Engheta, G. Eisenstein, A. J. Agranat, and M. Segev, "Control of light by curved space in nanophotonic structures," Nat. Photonics **11**, 664–670 (2017).
19. U. Leonhardt, "Perfect imaging without negative refraction," New J. Phys. **11**, 093040 (2009).
20. J. Perczel, T. Tyc, and U. Leonhardt, "Invisibility cloaking without superluminal propagation," New J. Phys. **13**, 083007 (2011).
21. U. Leonhardt and T. Philbin, *Geometry and Light: The Science of Invisibility* (Dover, 2010).
22. A. L. Besse, *Manifolds All of Whose Geodesics Are Closed* (Springer, 2012).
23. M. Šarbort, Non-Euclidean Geometry in Optics, Ph.D thesis (Masaryk University, 2013).
24. C. Sheng, H. Liu, Y. Wang, S. Zhu, and D. Genov, "Trapping light by mimicking gravitational lensing," Nat. Photonics **7**, 902–906 (2013).
25. C. Sheng, R. Bekenstein, H. Liu, S. Zhu, and M. Segev, "Wavefront shaping through emulated curved space in waveguide settings," Nat. Commun. **7**, 10747 (2016).
26. D. Wang, C. Liu, H. Liu, J. Han, and S. Zhang, "Wave dynamics on toroidal surface," Opt. Express **26**, 17820–17829 (2018).